

# Medical Image Synthesis via Monte Carlo Simulation

*James Z. Chen, Stephen M. Pizer, Edward L. Chaney, Sarang Joshi*  
Medical Image Display & Analysis Group, University of North Carolina, Chapel Hill, USA

## Abstract

A large number of test images and their “ground truth” segmentations are needed for performance characterization of the many image segmentation methods. In this work we developed a methodology to form a probability distribution of the diffeomorphism between a segmented template image and those from a population, and consequently we sample from these probability distributions to produce test images. This method will be illustrated by producing simulated 3D CT images of the abdomen for testing the segmentation of the human right kidney.

## 1. Introduction

This work explores a methodology for generating realistic, synthetic medical images for characterizing the performance of segmentation methods. It is intended to allow more effective validation and inter-comparison of algorithms that are designed to perform objective, reproducible segmentations of anatomical objects from medical images.

Test images intended for performance characterization should be able to represent the modality of interest and contain the “ground truth” segmentations, against which a particular segmentation method can be evaluated. Also, these images should represent statistical variations in the shape of target object across a population and span the range of image qualities found in a clinical setting. These properties mandate a large set of test images. In practice, however, it is a highly demanding task to define the ground truth segmentations for so many test images because 1) the manual segmentation by medical experts is a laborious and expensive process; 2) it has been shown that there exists a large variation even among the experts regarding the “correct” segmentations [Gerig 2001] due to subjective bias and the dependence on objectives.

A promising approach that could partially replace the costly performance evaluation procedures is to make use of synthetic images generated from simulations. Several statistical models of shape and appearance variability have been investigated and applied to perform various medical image analysis tasks. Examples are Active Shape Models (ASM) [Cootes 1994] and Statistical Deformation Models (SDM) [Rueckert 2001]. These methods can also be adapted to generate synthetic images for performance characterization by sampling the distribution of variability. But in building an ASM, a set of segmentations of the shape of interest is required as well as a set of landmarks that can be unambiguously defined in each sample shape. The manual identification of the point correspondences is a time-consuming task and is prone to the subjective bias. In the SDM method, this difficulty is removed by applying an automated nonlinear image registration. However, since the sample points in this model are distributed in the entire image volume, the computational complexity is non-trivial. In our method, the shape of the target object is represented via a limited number of automatically determined fiducial points. The computational efficiency is thus dramatically improved. Similar to the SDM method, the point correspondence across a population is established by a nonlinear, diffeomorphic image registration.

This work focuses on simulating the shape variability of the target anatomical object as observed across a population. The methodology will be laid out first, which includes the scheme of fiducial point shape representation, the training process, the shape analysis and the subsequent image synthesis. Then, this method will be applied to synthesize the CT images of the human abdomen as a demonstration. Although the illustration here is limited to a single-organ system, this method should be applicable for generating synthetic images of any anatomical structure in principle, including multi-organ complexes.

## 2. Methodology

### 2.1 Overview

Our method for generating realistic, synthetic medical images proceeds in two steps: training and sampling. In the training phase, the shape of the target object is studied, from which a distribution of its variation is derived. In the sampling phase, a large number of synthetic images can be produced by randomly sampling from the probability distribution.

For training purposes a set of clinical images containing the target object need to be collected, so as to capture the shape variations of the anatomical object of interest across the population. These images will be referred to as the training images  $\{I_t\}$ . One of  $\{I_t\}$  will be chosen as the template image  $I_0$ , and other images will be registered to  $I_0$  via a nonlinear, diffeomorphic warp function  $H_t$ :  $I_t \cong H_t(I_0)$ . Given a predefined segmentation  $S_0$  of the target object in  $I_0$ ,  $\{H_t(S_0)\}$  can be analyzed to find its probability distribution (referred to as the “normal shape domain”, or NSD). Artificial warp functions, and consequently the synthetic images and their segmentations, can then be generated by randomly sampling in the NSD. Details of this new method will be developed in the following sections.

### 2.2 Training Image Segmentation

Training defines the degrees of freedom that will characterize a typical object through observed shape variations across a population. The target object in a training image  $I_t$  can be recognized through an image segmentation  $S_t$ , which can be achieved via an automated image registration of  $I_t$  to the pre-labeled template image  $I_0$ . The large-scale fluid deformation method [Christensen 1997] is used in this work for the image registration. This method models  $I_0$  as a highly viscous fluid allowing for large-magnitude, nonlinear deformations, and the resulting registration function  $H_t$  (from  $I_0$  to  $I_t$ ) is represented as a diffeomorphic vector field. Before applying the fluid deformation method, the intensity and volume of each  $I_t$  needs to be normalized to that of  $I_0$ . Then,  $I_0$  is registered to  $I_t$  through a diffeomorphic function  $H_t$ :

$$I_t \cong H_t(I_0) \quad (1)$$

It is assumed here that the correspondence between these images established by  $\{H_t\}$  is the “true correspondence”. Some registration error may exist, but it should not be significant enough to affect the subsequent shape analysis.

Assuming the target object in  $I_0$  has been labeled *a priori* (denoted as  $S_0$ ), then that in  $I_t$  (denoted as  $S_t$ ) can thus be defined by applying the same warp function  $H_t$  on  $S_0$ ,

$$S_t = H_t(S_0) \quad (2)$$

Because the exact definition of the ground truth  $S_0$  is still an open research question, we propose to define the “ground truth”  $S_0$  by the consensus of an expert panel at this stage.

### 2.3 Fiducial Point Shape Representation

The shape of an object is defined as those aspects of its geometric conformation that are invariant under similarity transformations, for example, its topology. In this writing, the term “shape” can refer to either a specific instance of an object (for example, “the shape of a kidney in one CT image”) or a class of objects (for example, “the shape of the human right kidney”, or “shape and its variations”). Its exact connotation will be clear from the context. It is assumed that the shape of an object can be represented sufficiently by its surface when its conformation is simple, which is the case for many anatomic structures at a coarse scale level. A fiducial point shape representation made from a limited number of points on the surface will be developed next to represent an object’s shape according to its variation in the training set. The shape analysis then becomes the study of the displacement distributions of these points.

Given a predefined template shape  $S_0$ , and a set  $\{H_t\}$  that registers  $I_0$  to  $\{I_t\}$ , the various shapes of the object of interest in  $\{I_t\}$  can be represented by  $(S_0, \{H_t\})$ . Assume that each  $H_t$  can be encoded into the displacements of a limited number of points, from which another deformation field  $H'_t$  can be constructed to reproduce the deformation around  $H_t(S_0)$ . Then the representation of the various shapes is further simplified to the locations of these individual points and their corresponding displacements. The algorithm employed here to construct  $H'_t$  from a set of points and their displacements has been developed under the fluid deformation model and has been implemented as the “landmark fluid deformation” function in the fluid deformation program [Joshi 2000]. This function takes the initial and terminal locations of a set of points as the input, and generates a diffeomorphic deformation vector field that drives each point from its initial location to its destination.

This set of points on the surface of  $\mathcal{S}_\theta$  is named the “fiducial points”, denoted by  $\{\mathbf{F}_m\}$ , ( $m \in [1, M]$ ,  $M$  being the total number of fiducial points in the representation). In the extreme case of including all points on the surface of  $\mathcal{S}_\theta$ , we would have an enumerative representation of the surface. However, since the locations of these points are highly correlated due to the biological nature of the target object, some of these points are redundant in this representation and can be eliminated without losing significant information. The fiducial points predominantly reside at salient geometric and/or intensity features of an image.

An iterative procedure has been developed to find an optimal set of fiducial points in representing the shape of an anatomical object adequately and efficiently such that, on the average over all training samples, the difference between  $\mathbf{H}_t$  and  $\mathbf{H}'_t$

$$\frac{1}{T \cdot N_0} \sum_{t=1}^T \sum_{x \in \mathcal{S}_\theta} |H_t(x) - H'_t(x)| \quad (3)$$

is reduced below a predefined threshold on the surface of  $\mathcal{S}_\theta$ , where  $N_0$  is the number of voxels on the surface of  $\mathcal{S}_\theta$  and  $T$  is the total number of training samples. A surface curvature based geometric screening can be employed to initialize the seed point set – assuming large surface curvature implies important shape conformation, the first few points with the highest surface curvature are selected to define the initial fiducial point set  $\{\mathbf{F}_m\}$ . Then the following algorithm can be applied to each training case  $\mathbf{I}_t$  ( $t \in [1, T]$ ) to find the optimal fiducial point selection.

1. Apply the training warp function  $\mathbf{H}_t$  on  $\{\mathbf{F}_m\}$  to get the warped fiducial points:  $\mathbf{F}_{m,t} = \mathbf{H}_t(\mathbf{F}_m)$ ;
2. Reconstruct the diffeomorphic warp field  $\mathbf{H}'_t$  for the entire image volume based on the displacements  $\{\mathbf{F}_{m,t} - \mathbf{F}_m\}$ ;
3. Locate the point  $\mathbf{p}_t$  on the surface of  $\mathcal{S}_\theta$  that introduces the largest discrepancy between  $\mathbf{H}_t$  and  $\mathbf{H}'_t$ :  $\mathbf{H}_t(\mathbf{p}_t) - \mathbf{H}'_t(\mathbf{p}_t) = \max\{|\mathbf{H}_t(\mathbf{x}) - \mathbf{H}'_t(\mathbf{x})|\}$ , where  $\mathbf{p}_t, \mathbf{x} \in$  the surface of  $\mathcal{S}_\theta$ ;
4. In the point set  $\{\mathbf{p}_t\}$  established from all training images, find the point  $\mathbf{p}$  that introduces the largest discrepancy in  $\{\mathbf{H}_t(\mathbf{p}_t) - \mathbf{H}'_t(\mathbf{p}_t)\}$  and add it to the fiducial point set:  $\{\{\mathbf{F}_m\}, \mathbf{p}\} \Rightarrow \{\mathbf{F}_m\}$ ;
5. Loop back to step 1 until an optimization criterion is reached.

The optimization criterion can take various forms and one example will be demonstrated in *Section 3*.

#### 2.4 The Normal Shape Domain & Its Validation

Denote by  $\vec{\mathbf{f}}_0$  the collective coordinates of the fiducial point set  $\{\mathbf{F}_m\}$ ,

$$\vec{\mathbf{f}}_0 = ((x_{f_1}, y_{f_1}, z_{f_1}), (x_{f_2}, y_{f_2}, z_{f_2}), \dots, (x_{f_M}, y_{f_M}, z_{f_M})) \quad (4)$$

and  $\vec{\mathbf{f}}_t$  the displaced fiducial points  $\{\mathbf{F}_{m,t}\}$  ( $t = 1, 2, \dots, T$ ). So

$$\vec{\mathbf{f}}_t = \mathbf{H}_t(\vec{\mathbf{f}}_0) \quad (5)$$

The object’s shape in  $\mathbf{I}_t$  can be represented by  $\vec{\mathbf{f}}_t$  and the subsequent shape analysis will be on  $\{\vec{\mathbf{f}}_t\}$ .

$\vec{\mathbf{f}}_t$  is a single point in a  $3M$  dimensional space ( $M$  being the total number of fiducial points in the shape representation). A set of  $T$  training shapes gives a cloud of  $T$  points in this  $3M$ -D space. Assume that these points lie within some region of the space, which is named the “normal shape domain” (NSD). Every  $3M$ -D point within this domain will give a shape definition  $\vec{\mathbf{f}}$  that complies with those in the original training set. Thus new shapes can be generated systematically by sampling in this NSD. Also assuming that the NSD is approximately ellipsoidal, we can calculate its center and its major axes to give an analytical definition.

For a set of  $T$  training samples represented by  $\{\vec{\mathbf{f}}_t\}$ , the mean shape is

$$\langle \vec{\mathbf{f}} \rangle = \frac{1}{T} \sum_{t=1}^T \vec{\mathbf{f}}_t \quad (6)$$

The principal axes of the  $3M$ -D ellipsoid can be calculated by applying a principal component analysis to the deviation in the data from the sample mean:

$$d\vec{\mathbf{f}}_t = \vec{\mathbf{f}}_t - \langle \vec{\mathbf{f}} \rangle \quad (7)$$

Each principal axis gives a significant mode of variation, in which the fiducial points tend to move collectively as the shape varies. These principal axes are described by the unit eigenvector  $\{\bar{p}_k\}$  ( $k = 1, 2, \dots, 3M$ ) of the covariance matrix  $S$  formed from the deviations:

$$S\bar{p}_k = \lambda_k \bar{p}_k \quad (8)$$

Most of the variation can usually be explained by a small number of modes  $n$ . This means the  $3M$ -D ellipsoid can be approximated by an  $n$ -dimensional ellipsoid, and the original ellipsoid has a relatively small width beyond these  $n$  dimensions.

In order to assess the validity of the  $n$ -dimension NSD, another set of clinical images  $\{I_v\}$  of the same class but independent of  $\{I_t\}$  will be used. For each  $I_v$ , apply the fluid deformation registration method to register it with  $I_0$  via the warp function  $H_v$ . Then the corresponding displacements of the fiducial points  $\{H_v(F_m) - F_m\}$  will be reconstructed by using only the major modes defining the current NSD. Denote the reconstructed shape as  $\bar{f}_v$ .

Then,

$$\begin{aligned} \bar{f}_v &= \langle \bar{f} \rangle + \sum_{k=1}^n c_{v,k} \cdot \bar{p}_k \\ c_{v,k} &= \min(3\sqrt{\lambda_k}, (H_v(\bar{f}_0) - \langle \bar{f} \rangle) \cdot \bar{p}_k) \end{aligned} \quad (9)$$

From this, a diffeomorphic deformation field ( $H'_v$ ) for the entire image volume can be computed from  $(\bar{f}_0, \bar{f}_v)$  by using the landmark fluid deformation function introduced before. Then both  $H_v$  and  $H'_v$  are applied to the template shape  $S_0$ :  $H_v(S_0)$  and  $H'_v(S_0)$ , and these warped segmentations are compared, from which the assessment of the current NSD can be drawn. The NSD derived from the training process is validated if the shapes in  $\{I_v\}$  can be explained adequately, that is, they also fall into this NSD. An example of this validation process will be presented in Section 3.

### 2.5 Realistic, Synthetic Image Generation

Each point in the NSD can be reached by taking the mean shape and adding a linear combination of the eigenvectors. Therefore, a new shape complying with those training samples is

$$\bar{f}_s = \langle \bar{f} \rangle + \sum_{k=1}^n b_k \cdot \bar{p}_k \quad (10)$$

where  $b_k$  is the component coefficient of  $\bar{p}_k$ . As the variance of each mode  $\bar{p}_k$  is  $\lambda_k$ , suitable limits are typically of the order of

$$-3\sqrt{\lambda_k} \leq b_k \leq 3\sqrt{\lambda_k} \quad (11)$$

From the original and the displaced fiducial points  $(\bar{f}_0, \bar{f}_s)$ , a deformation field ( $H_s$ ) can be obtained by applying the landmark fluid deformation function. A synthetic image  $I_s$  and its ‘‘ground truth’’ segmentation will then be defined by

$$\begin{aligned} I_s &= H_s(I_0) \\ S_s &= H_s(S_0) \end{aligned} \quad (12)$$

A large number of realistic, synthetic images with known ground truth segmentations can be thus produced and used for characterizing the performance of the image segmentation methods.

## 3. Application: Synthetic Images of the Human Right Kidney

### 3.1 Training Image Segmentation

A pool of 36 clinical CT images  $\{I_t\}$  was prepared and one of them was selected as the template  $I_0$ , which has clear kidney region, low noise, minimal breathing artifacts and is close to the mean geometric conformation of all the training samples. The right kidney in  $I_0$  was then carefully segmented by medical experts and was used as the ground truth  $S_0$ . For each training image  $I_t$ , its intensity was normalized to that of the template  $I_0$ , and its resolution

was resampled to  $2mm \times 2mm \times 2mm$  via trilinear interpolation. To improve the convergence of registration, the MIRIT program [Maes 1997] was applied first to find the similarity transformation between each  $(I_0, I_t)$  pair.

As image quality varies, parameters in the fluid deformation program were fine-tuned in each case to give the best registration between  $I_0$  and  $I_t$ , as judged by visual inspection. The tri-orthogonal views of one training case are shown in *Fig. 1*. The contour superimposed over each image indicates the segmentation of the kidney – the manual segmentation for the template and the warped segmentation for the training image.

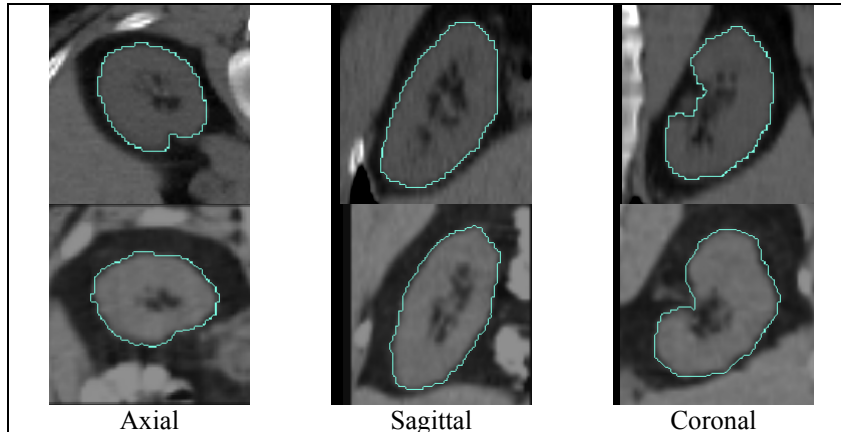


*Fig. 1: Training image segmentation: the template (1<sup>st</sup> row) and one training sample (2<sup>nd</sup> row).*

### 3.2 Fiducial Point Shape Representation

The algorithm developed in *Section 2.3* was applied to find the optimal point set for this data. The optimization criterion was taken from a previous independent study [ref], in which a comparison was made between two human raters' manual segmentations on a subset of the human kidney CT images used in this work. It was found that the average volume overlap between these two manual segmentations was 94.0%, and the average surface distance was 1.2mm apart, as measured by VALMET. Thus the iterative procedure was terminated when, on the average over all training samples, the similarity between  $H_t(S_0)$  and  $H'_t(S_0)$  surpassed the statistics from the human raters' comparison. In the fiducial point set initialization, a geometric screening selected the top 32 points with the highest surface curvature. The progress of optimization is graphed in *Fig. 2*.

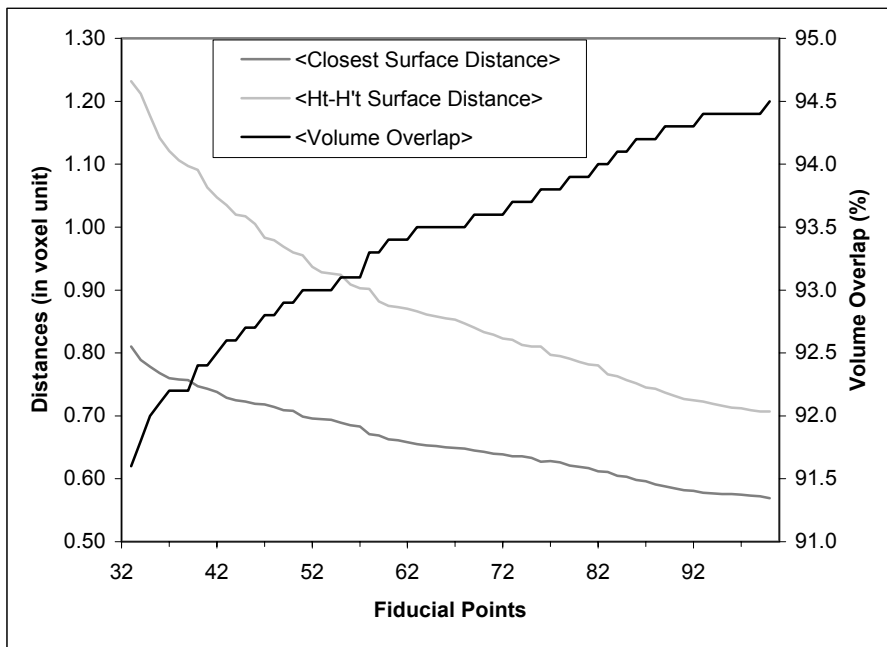


Fig. 2: Fiducial point set optimization for the human right kidney.

In this chart, each of the three statistical indices has been averaged over all 36 training samples. Both surface distance measurements are the averaged magnitude over all the voxels on the surface. The curve in light gray (labeled “<math>\langle H\_t - H'\_t \text{ Surface Distance} \rangle</math>”) shows the average point-wise (according to the diffeomorphisms) error between  $H_t$  and  $H'_t$  on the surface of kidney. The curve in darker gray (labeled “<math>\langle \text{Closest Surface Distance} \rangle</math>”) shows the averaged nearest surface distance from every point on surface of  $H_t(S_\theta)$  to that of  $H'_t(S_\theta)$ , so it is necessarily lower than the light gray curve. The curve in black gives the volume overlap between these two warped segmentations. The last two indices are calculated by the VALMET program [Gerig 2001], which compares and evaluates a pair of segmentations. Both distance measurements are in voxel units, and their ordinate is on the left. The volume overlap is measured in percentage, and its ordinate is on the right. The behavior of these curves is as expected – as more points are added into the fiducial point set, the average volume overlap increases monotonically and the distance measurements decrease correspondingly.

In representing the human right kidney, the volume overlap index has already exceeded 90% when only about 30 fiducial points are selected. Intuitively, this few points can hardly represent a shape in detail even for a simple 3D object. In segmentation comparison, the volume overlap measurement alone is sometimes misleading and should be used with great caution. We therefore report the average surface distance index in combination with this volume overlap index, and we sometimes even include the quartile statistics for more detailed analysis.

Applying the optimization criteria, the fiducial point shape representation for the human right kidney was established to comprise 88 points on the surface of  $S_\theta$ , with  $\langle \text{Volume Overlap} \rangle = 94.2\%$ ,  $\langle \text{Closest Surface Distance} \rangle = 0.591$ , and  $\langle H_t - H'_t \text{ surface distance} \rangle = 0.743$ .

### 3.3 Normal Shape Domain

MATLAB was used for the principal component analysis. Although the covariance matrix in this case was a 264-D ( $3 \times 88 = 264$ ) square matrix, its rank was only 35, because there were only 36 training samples in this study. Therefore, only the first 35 modes were non-trivial and the NSD in this model case was defined by the first seven modes (see *Table 1*). They covered more than 88% of the total variance observed in the training samples. In *Fig. 3*, the first three modes are shown at different variations.

Mode	Variance ( $\lambda_k$ )	Coverage (%)
1	370.59	59.07
2	177.33	11.51
3	142.59	8.45
4	81.76	3.66
5	52.21	2.81
6	47.76	1.57
7	31.33	1.34

*Table 1: Major modes of kidney shape variation.*

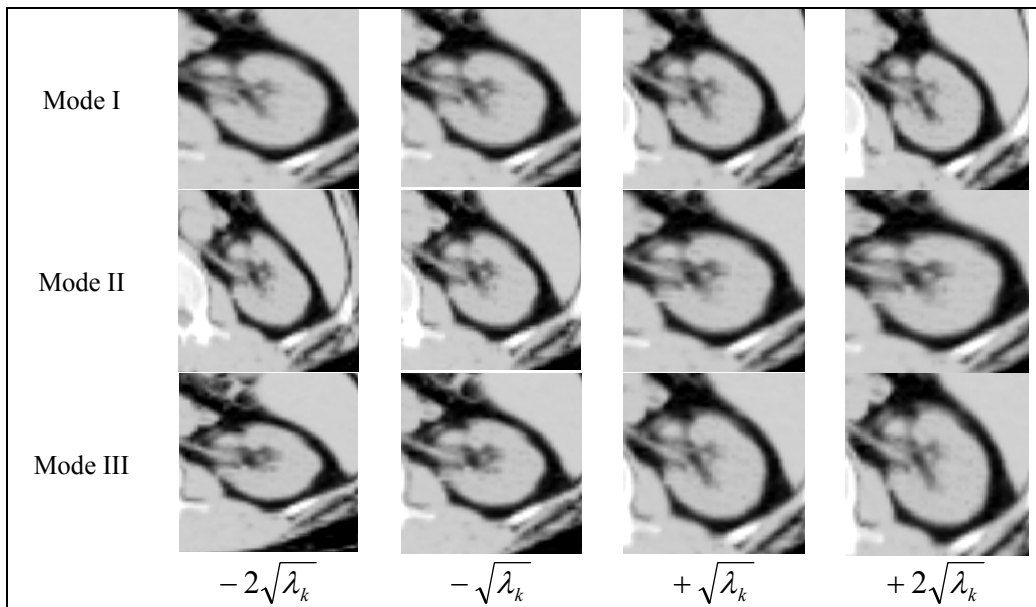


*Fig. 3: First three modes at different variations.*

To validate the NSD derived from the principal components analysis, four clinical CT images were used and they will be referred to as  $\{I_{V1}, I_{V2}, I_{V3}, I_{V4}\}$ . Following the validation scheme outlined in *Section 2.4*, the warped segmentation pair  $(H_v(S_\theta), H'_v(S_\theta))$  in each case was compared by the volume overlap and the average surface distance metrics evaluated by VALMET. The result is tabulated in *Table 2*. To put these numbers into perspective, the same procedure had been applied to all the training samples  $\{I_i\}$ , and the average value was taken for each of these evaluation metrics. It was found that, among all the training cases, the average volume overlap between  $H_v(S_\theta)$  and  $H'_v(S_\theta)$  was 90.4%, with a standard deviation (st.d.) of 1.7%; and the average surface distance was 0.874, with st.d. being 0.17. In every validation case, the difference of each metric ( $D_{volume}$  and  $D_{surface}$  in the table) from its average value was also measured by the corresponding standard deviation (“+” means better than average, “-” means inferior).

Case	Volume Overlap	( $D_{volume}$ in st.d.)	Surface Distance	( $D_{surface}$ in st.d.)
$I_{V1}$	92.1%	(+1.000)	0.728	(+0.859)
$I_{V2}$	92.4%	(+1.176)	0.759	(+0.676)
$I_{V3}$	88.4%	(-1.176)	0.902	(-0.165)
$I_{V4}$	89.6%	(-0.471)	1.008	(-0.788)

Table 2: Evaluation metrics for human right kidney NSD validation.

From Table 2, we see that the kidney shape in the case  $I_{V1}$  and  $I_{V2}$  have been thoroughly interpreted by the NSD, with both the volume overlap percentage and the average surface distance measurements being better than the average of those training samples. As for the cases  $I_{V3}$  and  $I_{V4}$ , even though the statistics are not as spectacular, the surface distance evaluation metrics falls within about one standard deviation from its average value.

### 3.4 Synthetic Image Generation

An arbitrary large number of synthetic human kidney CT images can now be produced from the current system. One such image is shown in Fig. 4, in comparison with the template. Note that the kidney object in the synthetic image takes a different shape from that of the template, but their background conformations (structures like liver, lung, spinal cord, and soft tissues) are very similar. Also, the intensity contrast and the noise level in these images are almost identical.

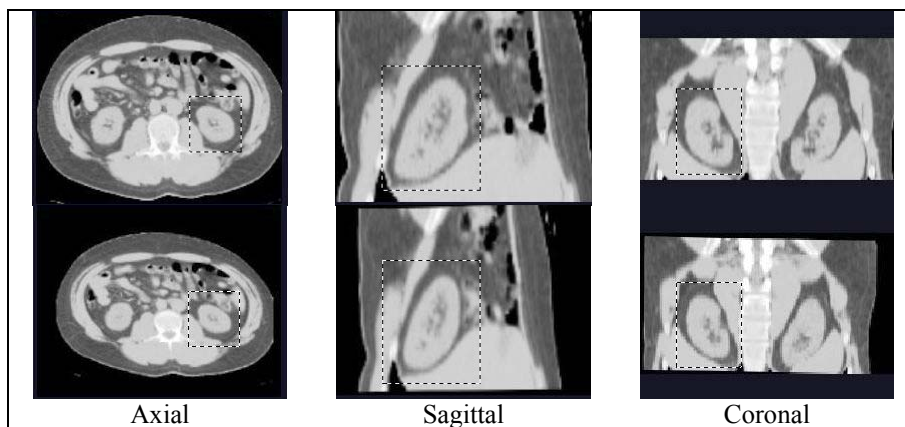


Fig. 4: The template (1<sup>st</sup> row) and one synthetic image (2<sup>nd</sup> row).

## 4. Discussion & Conclusion

In the model system of the human right kidney, only the kidney organ is modeled as an object (by  $S_\theta$ ) whereas all the other structures in the image are treated as the background intensity variation without any shape description. In order to produce truly realistic synthetic images for a large, multi-organ complex (for example, the entire abdominal region), the shape of each object in the complex needs to be studied to define an ensemble NSD of the system.

Also, because one single image  $I_\theta$  is used as the template in this example, all the synthetic images will inevitably share a similar background and intensity profiles. To alleviate this situation, a template transformation procedure can be employed – in generating a synthetic image  $I_s$ , a transformed warp function  $H_s H_t^{-1}$  can be used in place of  $H_s$ , with  $I_t$  as the template image instead of  $I_\theta$ . The characterization of this process is currently under investigation, and the result will be reported in a future publication.

To validate the NSD derived for the model system in Section 3, four validation cases have been used. The result shows that this NSD is able to explain the shape variations observed in these samples. Admittedly, a decisive conclusion regarding the validity of the current NSD cannot be drawn based on the tests from only a few cases. However, this does not prevent this method from generating synthetic images for performance characterization. The possibly limited scope of this NSD will be corrected and expanded by further training and testing, which will always be an interleaved on-going process.



In summary, a methodology has been developed to generate realistic, synthetic medical images via the Monte Carlo simulation for characterizing the performance of the image segmentation methods. As a demonstration, it has been applied to produce the synthetic CT images of the human right kidney. A test of the m-rep deformable model segmentation method [Pizer 2001] is currently in progress and its result will be reported in a separate publication.

## Acknowledgements

We sincerely appreciate the help and input from our colleagues during the development of this research work, with our special thanks to Dr. Keith Muller for the many insightful discussions on the statistical analysis and to Gregg Tracton for his superior technical support. The research reported here was carried out under the support of National Cancer Institute Grant P01 CA47982.

## References

- Christensen, G. E., S.C. Joshi and M.I. Miller (1997). "Volumetric Transformation of Brain Anatomy." IEEE Transactions on Medical Imaging **16**: 864-877.
- Cootes, T. F., A. Hill, C.J. Taylor, J. Haslam (1994). "The Use of Active Shape Models for Locating Structures in Medical Images." Image and Vision Computing **12(6)**: 355-366.
- Gerig, G., M. Jomier, M. Chakos (2001). "Valmet: A new validation tool for assessing and improving 3D object segmentation." Proc. MICCAI 2001, Springer LNCS 2208: 516-523.
- Joshi, S., M.I. Miller (2000). "Landmark Matching Via Large Deformation Diffeomorphisms." IEEE Transactions on Image Processing.
- Maes, F., A. Collignon, D. Vandermeulen, G. Marchal, P. Suetens (1997). "Multi-Modality Image Registration by Maximization of Mutual Information." IEEE-TMI **16**: 187-198.
- Pizer, S.M., J.Z. Chen, T. Fletcher, Y. Fridman, D.S. Fritsch, G. Gash, J. Glotzer, S. Joshi, A. Thall, G. Tracton, P. Yushkevich, and E. Chaney (2001). "Deformable M-Reps for 3D Medical Image Segmentation." IJCV, submitted.
- Rueckert, D., A.F. Frangi, and J.A. Schnabel (2001). "Automatic Construction of 3D Statistical Deformation Models Using Non-rigid Registration." MICCAI 2001, Springer LNCS 2208: 77-84.